A direct comparison of flow-by and flow-through capacitive deionization
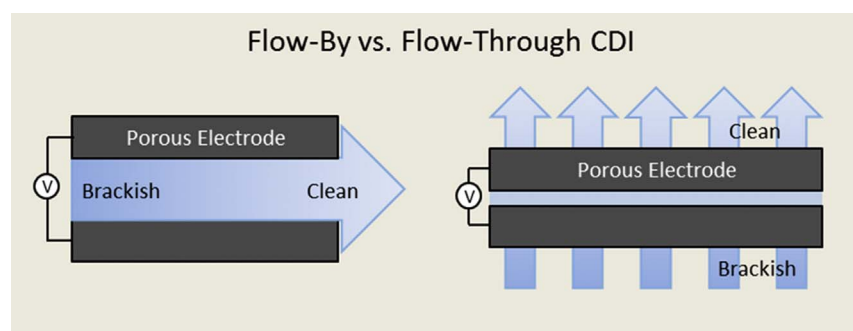
E. Marielle Remillard[a], Amit N. Shocron[b], John Rahill[a], Matthew E. Suss[b], Chad D. Vecitis[a,*]

[a] John A. Paulson School of Engineering and Applied Sciences, Harvard University, Cambridge, MA, USA
[b] Faculty of Mechanical Engineering, Technion – Israel Institute of Technology, Haifa, Israel

GRAPHICAL ABSTRACT

ARTICLE INFO

ABSTRACT

Capacitive deionization (CDI) is an electrochemical ion removal technique that could offer a lower energy or more selective alternative to reverse osmosis for water treatment applications. Over a dozen CDI cell architectures have been developed, but few studies have directly compared these designs for performance metrics such as ion adsorption rate and energy efficiency. Two of the most popular cell architectures include flow-by CDI, in which a feed stream flows parallel to two charged porous electrodes, and flow-through electrode CDI, in which the feed stream flows perpendicular to the electrodes. In this study, flow-by and flow-through CDI architectures were compared using commercially available electrode materials. Experimentally observed salt adsorption capacity (SAC), average salt adsorption rate (ASAR), and charge efficiency (Λ) was then compared to theoretical models over a range of voltage conditions (0.2–1.2 V), charge cycle times (1–60 min), and flow rates (10–30 mL min^{-1}). Cell architecture affected the SAC, ASAR, Λ, electrode stability, and oxidation rates for a given electrode material. Flow-by CDI tended to have higher SAC and better charge efficiency than flow-through CDI, yet flow-through CDI demonstrated a higher ASAR, particularly for shorter half-cycle times.

1. Introduction

Ion removal is an essential aspect of water treatment, and demand for ion removal processes has grow substantially in recent decades. The volume of freshwater produced by desalination has tripled since 2000 with over 16,000 facilities currently in operation worldwide. Many communities are turning to saline water supplies in response to growing water scarcity driven by population growth, climate change, and deteriorating freshwater quality. Meanwhile, ion removal in industrial applications has experienced similar growth. Demand for ultrapure water used in the manufacture of semiconductors, solar photovoltaics, and pharmaceuticals is growing around 8% per year[1]. Environmental regulations and efforts to recover resources from industrial wastewater streams contribute to this trend.

Despite growing demand, the current ion removal technologies will not be able to meet the water treatment needs of the future for two reasons. First, ion removal technologies are extremely energy intensive, and consequently have high associated financial and societal costs. Reverse osmosis, the most energy efficient ion separation technology available, can cost upwards of $0.18 m^{-3} [2] and requires 1–3 kWh m^{-3} for brackish water treatment. Moreover, there are limited opportunities to further reduce energy consumption using membrane based technologies beyond the current state-of-the-art[3]. Alternative processes for deionizing water exist, such as distillation or electrodialysis, but they struggle to compete in terms of cost and energy efficiency. Second, there is growing demand for processes that can selectively remove ions from water[4]. Current technologies are either non-specific in their removal of ions, for example physisorption, photocatalytic degradation, and membrane-based processes, or the systems must be uniquely designed, as in the case of ion exchange resins, incurring high cost[5]. An ideal water treatment technology would be energy efficient, affordable, easily adapted to treat a wide range of water sources, and could be easily tailored remove ions selectively.

Capacitive deionization (CDI) could provide a suitable alternative to the existing ion removal techniques due to its low energy consumption and potential for ion selectivity. This electrochemical technology uses a low-voltage electric field to separate ions from a solution in a two-step process; ions are stored in the electric double-layer of a porous electrode during water treatment, and ions can later be discharged into a waste stream regenerating the electrodes. CDI can require less energy to treat brackish water (< 3.5 g L^{-1}) than reverse osmosis, particularly when energy recovery is included[6–8]. This ultimately reduces environmental impact by decreasing greenhouse gas emissions and lowering operational cost. In addition, ions can be removed selectivity based on ion valence, size, and diffusivity [9,10]. This allows a single CDI design to be used in a wide range of water treatment applications and for the process to be continuously tuned during operation. Future applications could include water softening[11], Li$^+$ ion recovery from industrial processes[12–14], and nutrient enrichment for agriculture.

Over the past two decades, research into CDI has experienced rapid growth as scientists aim to harness the potential energy savings and ion selectivity. To date, more than a dozen cell architectures have been developed with the objective of optimizing energy efficiency[8], salt adsorption capacity[15], electrode regeneration[6], and ion removal rate[16]. Moreover, there have been hundreds of novel electrode materials created with similar objectives[17,18]. As a result of this rapid growth, however, it can be difficult to isolate factors that yield optimal performance. Few studies have directly compared cell architectures or considered the effect of cell architectures on electrode performance[19].

In an effort to better understand the influence of operational mode on CDI performance, a direct comparison of flow-through and flow-by CDI, the most commonly used cell architectures, was conducted using four types of electrode materials: carbon fiber (CF), carbon nanotubes (CNT), carbon nanofoam (NF), and activated carbon cloth (CC). Commercially available electrode materials were selected in order to allow other researchers to easily compare results. Each flow cell was designed to have comparable geometry, and the deionization performance was tested under a range of conditions including voltages from 0.2 to 1.2 V, half cycle times from 1 to 60 min, and flow rates from 10 to 30 mL min^{-1}. Finally, there are two notable differences between flow-by and flow-through CDI in this study. First, the electric field is perpendicular to flow in flow-by CDI, whereas in flow-through CDI they are parallel. Secondly, ion transport can be diffusion-limited in the flow-by cell architecture[20],while in the flow-through cell architecture, fluid advection transports ions sequentially through the electrodes.

2. Experimental

2.1. Materials

The NaCl for solution was obtained from BDH-VWR Analytical. Deionized (DI) water was produced by a Picotap laboratory faucet (Hydro Service and Supplies, Inc.). The peristaltic pump used in experiments was a Cole Palmer MasterFlex L/S model 755702 with MasterFlex 06509-16 Tygon E-lab tubing (E3603). The power source was an Agilent 3646A DC power supply (Santa Rosa, CA), and voltage and current were measured using Vernier software and sensors (Beaverton, OR). Conductivity was measured using an Orion Dura Probe 4 Electrode Conductivity probe with OrionStar A215 interface (ThermoFisher Scientific).

2.2. Electrode materials and characterization

Four commercially available carbon-based materials were used as CDI electrodes: carbon nanotube buckypaper (CNT; C-grade MWCNT, NanoTechLabs), carbon nanofoam (NF; Type II, MarkeTech International), and activated carbon cloth (CC; Spectracarb 2225 Type 900, Engineering Fiber Technologies). A second brand of activated carbon cloth (Kynol ACC-507-15, Kynol Europa GmbH) was also considered, however, the results were similar to CC. Kynol (K) material properties and CDI performance can be found in Appendix A. **SEM**: Material images were obtained using a Field Emission Scanning Electron Microscope (SEM) (Zeiss, UltraPlus or Ultra55, EHT = 2–5 kV). **Surface characterization** specific surface area (SSA) and micropore volume ($\forall_{mi}$) were obtained using a Micrometrics 3Flex TCD Surface Characterization Analyzer. Samples (0.05–0.5 g) were outgassed for 9 h (1 h at 90 °C followed by 8 h at 300 °C) and analyzed using the BET, T-point, BJH, and DFT methods using nitrogen gas. SSA was measured using BET. For BET calculations, the relative pressure was set using the Rouquerol BET plot such that the linear region had a p-value > 0.999. $\forall_{mi}$ was approximated from the BJH data by summing the pore volume for pores < 2 nm. **Sheet resistance/resistivity**: Four-point probe measurements were obtained for each sample using a custom probe (Haitao Zhang, Harvard University) with 1 mm probe spacing. Resistivity was computed by multiplying sheet resistance by the material thickness. **CV**: Cyclic voltammetry (CV) plots were produced with a CH instruments electrochemical analyzer using a 5 mM or 1 M NaCl solution, a Pt foil counter electrode, and an Ag/AgCl/1 M KCl working electrode. Prior to testing, the Pt electrode was cleaned via sonication in DI water, followed by electrochemical cycling in 0.5 M H$_2$SO$_4$ between − 0.23 and + 1.10 V at 100 mV s^{-1}[21]. CV scans were obtained for 0 to 1.0 V at 1, 5, 10, and 50 mV s^{-1}. 1 M NaCl was selected in order to ensure solution conductivity and to minimize electromigration of the ions[22]. Select CV plots are reported in Appendices A and B. **Chronopotentiometry**: Capacitance was measured via chronopotentiometry using an electrochemical analyzer (CH Instruments) in 1 M NaCl solution with Pt foil the counter electrode, and Ag/AgCl/1 M KCl as the reference electrode. CF, CNT, and NF samples were pretreated with 50% EtOH to improve wettability. Samples were scanned from 0 to 1.0 V at fixed current density of 0.1 to 0.5 A g^{-1}. Capacitance values are reported at 0.1 A g^{-1}. Additional details are available in Appendix B. **Contact angle**: The contact angle was measured with a Ramé Hart goniometer using DROPimage CA software, and the angle was measured using *ImageJ* (National Institute of Health). A 10 μL droplet of DI water was added to each sample surface. In instances where dynamic wetting was observed, the initial contact angle, measured < 5 s after droplet was added, was reported. Measurements were taken in three locations of each sample and averaged. Images are available in Appendix C. **XPS**: X-ray photoelectron spectroscopy (XPS) measurements were made with a Thermo Scientific K-Alpha XPS, ESCA. Oxygen content for each electrode material was determined using survey scans looking for elemental signatures between − 10 and
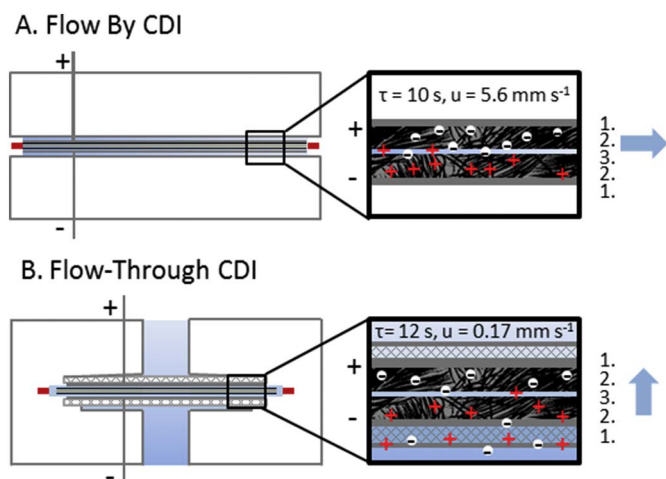
A. Flow By CDI

B. Flow-Through CDI

Fig. 1. Cell architectures. A. Flow-by CDI and B. Flow-through CDI cell architectures were designed to use 1. titanium current collectors, 2. carbon electrodes, and 3. PTFE membrane spacers. In flow-by mode, the electric field is perpendicular to the flow direction, whereas in flow-through, electric field and flow direction are parallel. In both designs, the fluid can flow through the interstices of the electrode and the spacer (85 μm) is predominantly used to separate electric charge. τ is the hydraulic residence time of the fluid and u is the superficial velocity in the flow cell (flow rate divided by cell volume not accounting for electrodes and spacer materials) at a flow rate of 20 mL min^{-1}. Image is not drawn to scale.

1350 eV (spot size = 400 μm, flood gun = on, auto height = ± 1000 μm, step = 50 μm, dwell time = 0.5 s, energy step size = 1.00 eV). The automated Enhanced Survey ID feature of *Avantage* (Thermo Fisher Scientific) was used to analyze the XPS survey spectra. Measurements were taken in three locations of each sample and the average oxygen content was reported. Sample XPS spectra can be found in Appendix D.

2.3. CDI apparatus

Custom acrylic flow cells were used to compare flow-by and flow-through operational modes, depicted in Fig. 1. In both cases, titanium (thickness = 0.127 mm) was used as the current collector, and the carbon electrodes were separated by a hydrophilic PTFE membrane (Omnipore, d_{pore} = 5 μm, thickness = 85 μm). The flow-by CDI apparatus consists of a rectangular compartment $29.5 \times 58.9 \times 2$ mm^3, while the flow-through CDI apparatus has a circular flow chamber 47 mm in diameter. The geometric shape (circle vs. rectangle) were selected in order to minimize dead spaces in the flow channels. For CDI testing, each electrode was cut to 1735 mm^2 either as a disk with diam. = 47 mm, or as a rectangle 29.5×58.9 mm^2. The average mass for an electrode pair depended on the electrode material due to differences in density and thickness: CF = 0.35 ± 0.01 g, CNT = 0.12 ± 0.00 g, NF = 0.37 ± 0.02 g and CC = 0.50 ± 0.01 g. Under most circumstances, electrodes were used for 6–24 h before being replaced. Porous plastic disks were used to support the titanium current collector and carbon electrode material (d = 47 mm). EPMD O-rings (McMaster Carr) and/or 1 mm thick rubber gaskets were used to prevent leaking. Images of the experimental flow cells can be found in Appendix E.

To compare performance for flow-by and flow-through cell architectures (Section 3.2), 292 mg L^{-1} (5 mM) NaCl was continuously pumped through the CDI unit using a peristaltic pump at a flow-rate of 20 mL min^{-1} unless otherwise specified. The NaCl solution was not de-aerated prior to experimentation in order to better simulate natural water resources. Conductivity of the effluent was recorded in 3 s intervals using the StarCom software. Single-pass mode was used for all tests; during operation, the NaCl solution was pumped from a 15 L reservoir, passed through the CDI unit and into a 40 mL fixed volume vessel where the effluent conductivity was recorded, and then finally

the solution was returned to the reservoir. Electrical potential was supplied to the CDI unit using a computer interface, and the voltage was limited to 1.2 V in order to minimize water splitting. Current and voltage were measured in 0.1 s intervals using Vernier LabPro sensors and LoggerPro software. For hydrophobic materials (CF, CNT, NF), the electrodes were primed with 1:1 v/v EtOH:H$_2$O (50% EtOH) in order to enhance wettability prior to experimentation. To do so, 0.5–2 mL of 50% EtOH were added directly to the dry electrode material and subsequently flushed with 50 mL of DI water followed by 25 mL of 292 mg L^{-1} NaCl using a peristaltic pump at a flow rate of 20 mL min^{-1}. No pre-treatment was used for the carbon cloth.

EIS: Electrochemical impedance spectroscopy (EIS) measurements were obtained *in situ* (i.e. by measuring the response in the CDI flow cells) using an electrochemical analyzer (CH Instruments). The carbon electrodes (CC,NF) served as the working and counter electrodes, and an Ag/AgCl/1 M KCl electrode was used for the reference. The reference electrode was inserted into the outlet of the flow cell. NF electrodes were pretreated with 50% EtOH to improve wettability. EIS spectra were obtained at three different flow rates: 10, 20, and 30 mL min^{-1} using 292 mg L^{-1} NaCl in single-pass mode. First, the flow cell was primed for 45 min at 10 mL min^{-1} to allow the system to reach equilibrium and the first spectrum was obtained. Next, the flow rate was adjusted and the CDI system was given 15 min to re-stabilize before taking each subsequent reading. The spectrum was measured three times at each flow rate, and frequencies, ω, ranged from 0.1 to 2×10^6 Hz at 10 mV AC. Results are shown in Appendix F.

2.4. CDI metrics

The following metrics were used to evaluate CDI performance [23]:

1. Salt Adsorption Capacity (SAC): Salt adsorption capacity describes the salt stored in the electrode for a given charge cycle. Voltage was cycled between 0 and 1.2 V for cycle times ranging from 2 to 120 min (where one cycle includes both the charging and discharging phase). The SAC for a given cycle time was computed as

$$SAC = \frac{\Phi^* \int_0^{t_{cycle/2}} |C(t)| dt}{m} \qquad (1)$$

   where Φ is the volumetric flow rate (L min^{-1}); C(t) is the difference between initial concentration and current concentration (mg L^{-1}) as a function of time, C_0-C; t represents time (min); and m is the combined electrode mass (anode + cathode) (g). The concentration is only integrated for the charging phase of the cycle, $t_{cycle/2}$. The values reported for SAC are the average of 6 cycles and expressed in units of mg g^{-1}. For long cycle times, the system reaches a state of equilibrium where salt is no longer removed during the charging cycle. In theory, the maximum salt adsorption capacity (mSAC), defined by electrode material properties, should equal the equilibrium salt adsorption capacity (eq-SAC).

2. Charge Efficiency (Λ): Charge efficiency is a unitless metric that describes the moles of salt removed per mole of electrons transferred between electrodes and is calculated as

$$\Lambda = \frac{F^* \Phi^* \int_0^{t_{cycle/2}} |C(t)| dt}{M^* \int_0^{t_{cycle/2}} I(t) dt} \qquad (2)$$

   where F is Faraday's constant (96,485 C mol^{-1}), M is the molar mass of the salt (g mol^{-1}), and I(t) is current (A) as a function of time (s).

3. Average salt adsorption rate (ASAR): Average salt adsorption rate describes how quickly salt is removed from the solution. It is computed from the SAC by dividing by the cycle time, t_{cycle} (min):

$$ASAR = \frac{SAC}{t_{cycle}} \qquad (3)$$

   ASAR is reported in units of mg g^{-1} min^{-1}.

4. Specific charge (Q): Specific charge describes the amount of charge stored per mass of electrode in units of C g^{-1} and is calculated as

$$Q = \frac{\int_0^{t_{cycle/2}} I(t)dt}{m} \qquad (4)$$

Here, the specific charge was calculated using the discharge current. In some instances it is more convenient to consider the number of electrons per gram instead; in this case, Q can be divided by F to get the number of moles of electrons per gram.

2.5. Improved modified-Donnan (i-mD) model

The i-mD model describes salt removal during the CDI process by assuming that the ions removed from solution are stored in the micropores within the electrodes, and that the concentration of ions stored within the micropore (c_{mi}) relates to the bulk concentration (c_{ma}) such that $c_{mi,i} = c_{ma}e^{(-z_i\Delta\Phi_D + \mu_{att})} = c_{ma}e^{(\Delta\Phi_D + E/c_{mi})}$. Here, the total micropore concentration, c_{mi}, is defined as $c_{mi} = c_{mi,+} + c_{mi,-}$, and therefore the expression for the total micropore concentration is $c_{mi} = 2c_{ma}e^{(E/c_{mi})}cosh(\Delta\Phi_D)$ for a univalent symmetric system. Initially, $\Delta\Phi_D = 0$, therefore we attain Eq. (5):

$$C_{mi,0} = 2 \cdot C_{ma} \cdot e^{\mu_{att}} \qquad (5)$$

where μ_{att} is the attractive potential of the electrode material. The attractive potential can be expressed as $\frac{E}{C_{mi,0}}$, where E is the image attraction energy (mM kT), and the attractive forces are inversely related to the ion concentration in the micropore, C_{mi}[24].

The ionic charge density (σ_{mi}, mM) inside the micropore is given by Eq. (6). It relates to the electronic charge (Q) through Eq. (7) and the applied potential (V) through Eq. (8):

$$\sigma_{mi} = \sqrt{C_{mi}^2 - 4 \cdot C_{ma}^2 \cdot e^{\frac{2 \cdot E}{C_{mi}}}} \qquad (6)$$

$$Q = 0.5 \cdot F \cdot v_{mi} \cdot \sigma_{mi} \qquad (7)$$

$$V = 2 \cdot V_T \left(sinh^{-1}\left(0.5 \frac{\sigma_{mi}}{C_{ma}} \cdot e^{\frac{-E}{C_{mi}}} \right) + \frac{F \cdot \sigma_{mi}}{(C_{st,0} + \alpha \cdot \sigma_{mi}^2) \cdot V_T} \right) \qquad (8)$$

Here, C_{st} is the zero charge volumetric Stern layer capacitance (F m^{-3}), α is an empirical fitting factor (F m^3 mol^{-2}), and V_T is the thermal voltage (RT F^{-1}).

The SAC, Eq. (9), and Λ, Eq. (10), can then modeled as

$$SAC = 0.5 \cdot M_u \cdot v_{mi}(C_{mi} - C_{mi,0}) \qquad (9)$$

$$\Lambda = \frac{(C_{mi} - C_{mi,0})}{\sigma_{mi}} \qquad (10)$$

Fitting parameters for the model typically include E, $\forall_{mi}$, C_{st}, and α. Here, we used E = 250–300 kT·mol m^{-3} for both materials as it is a reasonable value for carbon material with 2 nm average micropores [24]. The micropore volume was taken from BJH measurements (NF $\forall_{mi}$ = 0.27 mL g^{-1}, CC $\forall_{mi}$ = 0.44 mL g^{-1}). C_{st} and α were fit to Q vs. V data obtained using flow-by CDI. For NF, C_{st} = 0.170 GF m^{-3} and α = 35 F m^3 mol^{-2}. For CC, C_{st} = 0.200 GF m^{-3} and α = 30 F m^3 mol^{-2}. The i-mD model was only used to analyze the equilibrium SAC data, and for those experiments, there is no strong evidence that fixed chemical charge (such as carboxyl surface groups) influenced the CDI results. The electrodes were replaced every 12 h of operation, and little to no peak inversion was observed in the conductivity profile as shown in Appendix G.

3. Results

3.1. Electrode characterization

The four carbon electrode materials differed in both morphology and electrochemical performance. SEM images, shown in Fig. 2A,
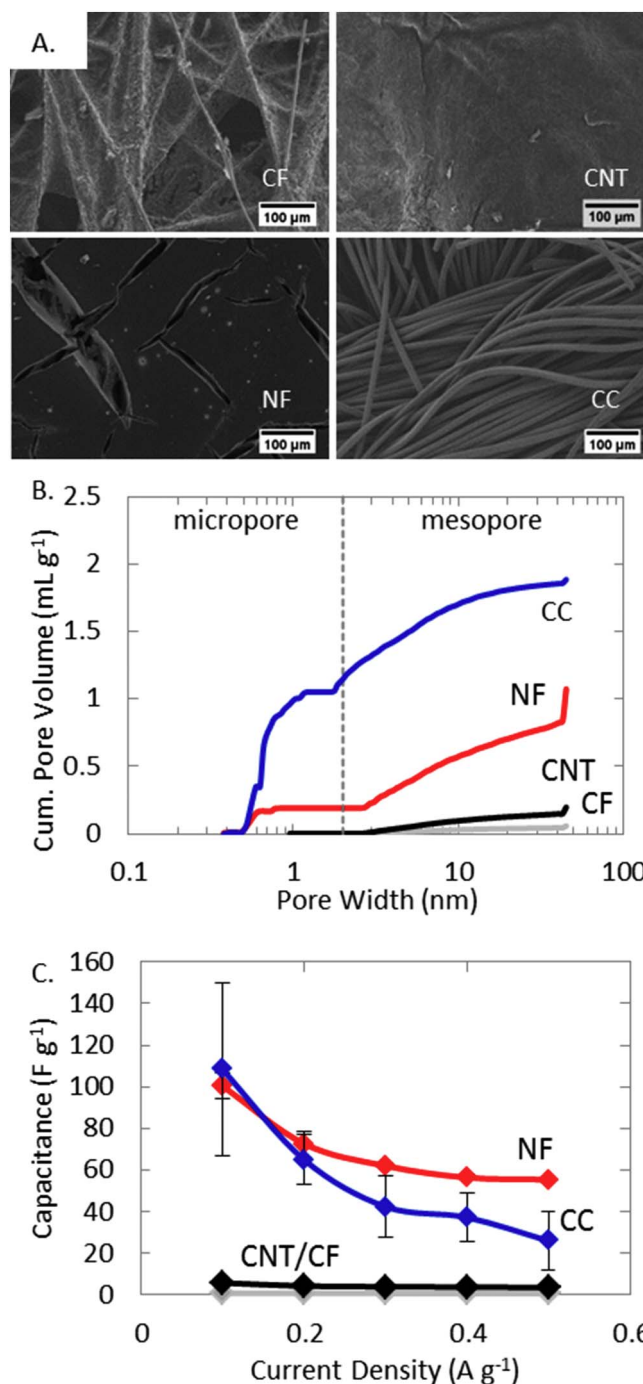

Fig. 2. Material characteristics. A. SEM images of each material, B. DFT pore size distribution, and C. specific capacitance measured in 1 M NaCl. N = 3, error bars show standard deviation.

highlight the differences in macropore structure. The CF, NF, and CC electrodes all have visible pores or cracks on the order of 10–100 μm, while the CNT buckypaper has pores that are three orders of magnitude smaller (~10–100 nm). At high magnification (50 kx), additional features were observed. The CF appeared to have amorphous μm-scale particles coating the surface of the carbon fibers, and the randomly-oriented network of CNT fibers ($\bar{d}$ = 22 ± 9 nm) could be observed in the CNT buckypaper. Meanwhile, nm-scale pores were easily visible in the NF and CC samples which appear to have dense, foam-like structures at high magnification. Additional SEM images, including higher magnification and cross sections, are available in Appendix H.

BET surface area measurements indicated that the CC had the

Table 1
Carbon electrode material properties.

Property	CF	CNT	NF	CC
Thickness (μm)	150 ± 10	90 ± 10	210 ± 30	560 ± 20
SSA[†] (m² g⁻¹)	42.6 ± 0.5	132 ± 1	705 ± 6	2980 ± 10
$\forall_{mi}$[†] (mL g⁻¹)	0.02	0.07	0.27	0.44*
Capacitance (F g⁻¹)	0.9 ± 0.2	5.8 ± 0.4	100 ± 6	110 ± 40
Resistance (Ω □⁻¹)	0.24 ± 0.01	0.35 ± 0.03	0.43 ± 0.02	3.93 ± 0.5
Resistivity (mΩ cm)	3.6 ± 0.3	3.0 ± 0.4	9.0 ± 1.0	220 ± 30
Contact angle (°)	140 ± 10	142 ± 2	48 ± 20	0 ± 0
at% O (%)	0.8 ± 1.0	0.9 ± 0.1	2.1 ± 0.2	6.6 ± 1.2
SEM features (500 ×)	100s μm pores	No porosity visible	10–100 μm cracks	13 μm wide fibers
SEM features (50k ×)	10s nm features	10s to 100s nm pores	< 10 nm pores	< 300 nm pores

Note: N = 3 except [†]N = 1, ± standard deviation, capacitance at 0.1 A g⁻¹, *t-plot value = 0.60 mL g⁻¹.

highest specific surface area (2980 ± 10 m² g⁻¹) followed by the NF (705 ± 6 m² g⁻¹), CNT (132 ± 1 m² g⁻¹) and finally CF (42.6 ± 0.5 m² g⁻¹). Furthermore, high surface area corresponded to high micropore volumes and high specific ions. Fig. 2B shows the DFT pore size distribution for each material and Fig. 2C shows specific capacitance over a range of current densities. Further information about

the electrochemical performance of each material was obtained from CV plots (see Appendix B), which indicate the presence of faradaic reactions taking place in the CF at 0.5 V, and strong water splitting peaks at 1.2 V in the CF and CNT samples.

The resistivity and wettability of each material was also characterized. Resistivity values ranged from 220 ± 30 mΩ cm⁻¹ for the CC to 3.0 ± 0.4 mΩ cm⁻¹ for the CNT. Meanwhile, based on contact angle measurements, the CC was most hydrophillic (0° ± 0°), again followed by the NF (48° ± 18°), CF paper (140° ± 10°), and finally the CNT buckypaper (142° ± 2°). Higher oxygen content in CC (6.6%O) and NF (2.2%O) electrodes likely enhanced wettability, although, oxygen content increased for all materials after charge-discharge cycling in the CDI cell (see Appendix D). Material properties are summarized in Table 1.

3.2. CDI performance

Batch-mode tests were used as an initial screen to determine the efficacy of each electrode material, see Appendix I. Based on the low salt adsorption of the CF and CNT materials (≤ 1.0 mg g⁻¹), only the NF and CC materials were used in further tests. Poor performance of the CF and CNT materials can be attributed to their low specific micropore volume (mL of micropores per g of material), a material feature which strongly correlates with salt adsorption capacity[25]. Furthermore, CF and CNT had the lowest oxygen content of the electrodes tested. Oxygen content influences the PZC of the material, and thus will affect the cathode ion adsorption. For example, cathodic materials with higher oxygen content exhibit superior CDI performance due to
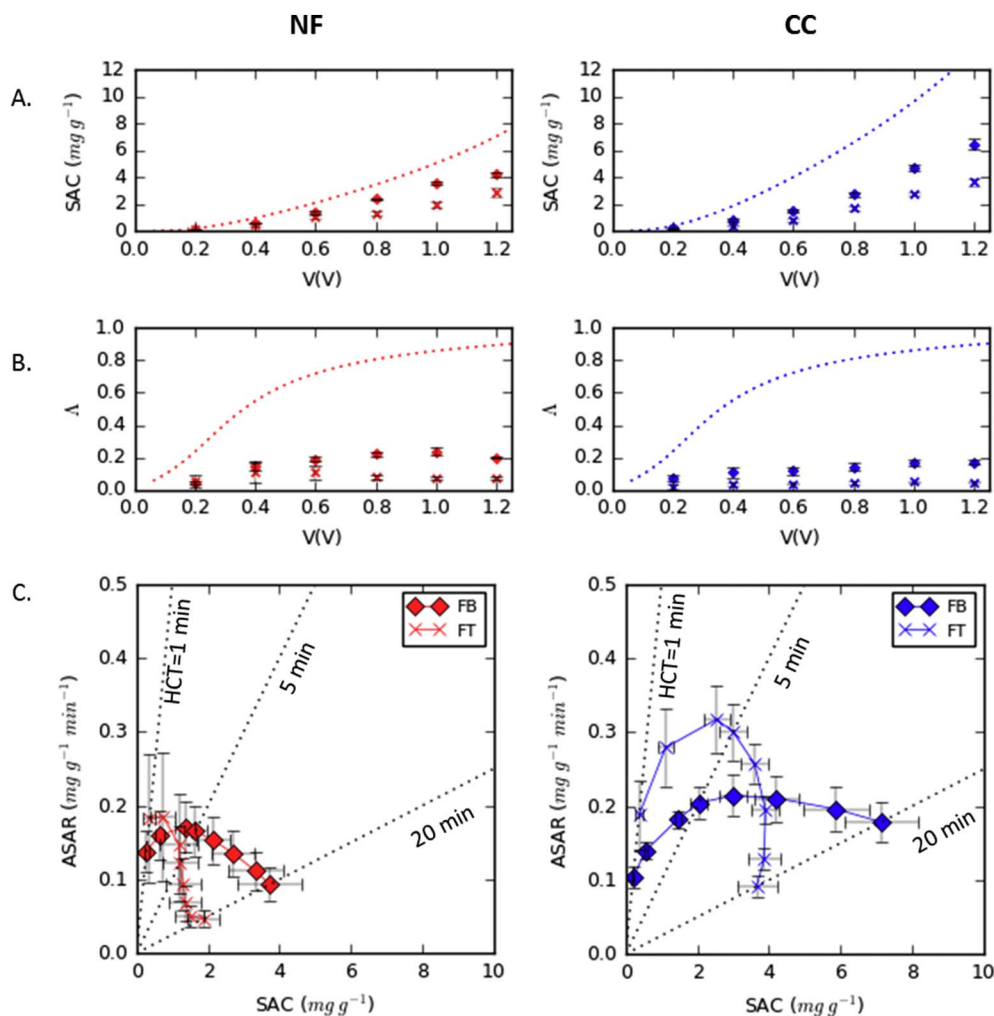

Fig. 3. A. Salt adsorption capacity (SAC), and B. charge efficiency (Λ) were higher using the flow-by CDI (◇) compared to the flow-through CDI (x) for both the NF (red) and the CC (blue). The dashed line shows expected theoretical performance using the i-mD model. The model fitting parameters are as follows: NF: E = 250 kT mol m⁻³, α = 35 F m³ mol⁻², C_{st} = 0.170 GF m⁻³, v_{mi} = 0.27 mL g⁻¹; CC: E = 300 kT mol m⁻³, α = 30 F m³ mol⁻², C_{st} = 0.200 GF m⁻³, v_{mi} = 0.44 mL g⁻¹. C. Kim-Yoon plots for NF and CC show the relationship between the amount of salt removed (SAC) and the salt adsorption rate (ASAR). Each data point represents the average SAC and ASAR for a single HCT, and HCT increases from left to right. Select HCT are labeled for reference. All charging and discharging times were equal, Φ = 20 mL min⁻¹, N = 3, error bars show standard deviation. (For interpretation of the references to color in this figure legend, the reader is referred to the web version of this article.)

improved charge transfer and less co-ion repulsion[26].

The difference in salt removal between flow-by and flow-through CDI was then characterized under equilibrium conditions. Under these conditions, in which voltage is applied continuously for 1 h, the eq-SAC should depend only on the properties of the electrode material[23]. The eq-SAC was measured for NF and CC over a range of voltages (0.2–1.2 V), and the results, displayed in Fig. 3A, were compared to the expected theoretical values according to the improved-modified Donnan (i-mD) model[24]. An example of the raw data including applied potential, response current, and concentration over time can be found in Appendix G. For both NF and CC, the eq-SAC was higher for flow-by than flow-through CDI, with greater salt adsorption occurring with higher applied potentials. At 1.2 V, the eq-SAC for NF-FB (4.2 ± 0.2 mg g^{-1}) was 31% higher than NF-FT (2.9 ± 0.3 mg g^{-1}). Similarly, eq-SAC for CC-FB (6.4 ± 0.4 mg g^{-1}) was 48% higher than the eq-SAC for CC-FT (3.7 ± 0.3 mg g^{-1}). Nevertheless, for both materials and both cell architectures, the eq-SAC was lower than predicted by the i-mD model. Additionally, both flow-by and flow-through designs had low charge efficiency (< 20%) as shown in Fig. 3B. Charge efficiency improved slightly with increasing applied voltage, but it was far lower than predicted by the i-mD model which anticipated charge efficiencies > 80% at 1.2 V. Moreover, flow-by CDI removed salt more efficiently than flow-through CDI regardless of electrode material. Although identical electrode materials were compared in each system, differences in flow cell impedance and parasitic side reactions likely contributed to the observed discrepancy in eq-SAC using flow-through vs. flow-by CDI.

Next, the salt adsorption capacity (SAC) was compared to the average salt adsorption rate (ASAR) over a range of half-cycle times (1–20 min) as shown in Fig. 3C. Values in the top right quadrant of the graph show optimal performance in which both salt adsorption capacity and rate of salt adsorption are maximized[27]. Maximal salt removal was achieved using flow-by CDI for both NF (3.72 mg g^{-1}, HCT = 20 min) and CC (7.13 mg g^{-1}, HCT = 20 min). Using the flow-through architecture, the maximum SAC was 45 to 50% lower (NF, 1.87 mg g^{-1}, HCT = 20 min; CC, 3.90 mg g^{-1}, HCT = 10 min). On the other hand, the rate of salt removal was faster using the flow-through design for short HCT, < 2 min for NF and < 5 min for CC. The maximum ASAR for NF reached 0.18 mg g^{-1} min^{-1} (HCT = 2 min) compared to 0.17 mg g^{-1} min^{-1} (HCT = 3 min) for flow-by CDI. Similarly, ASAR for CC was higher using flow-through CDI (FT = 0.32 mg g^{-1} min^{-1}, HCT = 4 min; FB = 0.21 mg g^{-1} min^{-1}, HCT = 7 min). Faster ion kinetics were expected for the flow-through cell architecture[16], however, for both electrode materials, ASAR decreased rapidly with increasing HCT. Furthermore, flow rate (10–30 mL min^{-1}) strongly influences CDI performance; faster flow rates enhance SAC and ASAR in the flow-by architecture, and faster flow rates improve ASAR but have little effect on SAC for the flow-through design; results can be seen in Appendix J. The effect of flow rate on SAC and ASAR were also reported by Kim et al. using an membrane capacitive deionization (mCDI), and Liu et al. using a flow-through design. Using mCDI, higher flow rates led to increased ASAR flow rates between 1 to 4 mL min^{-1}[27]. Meanwhile, for flow-through CDI operating at flow rates from 20 to 80 mL min^{-1}, optimal performance increased from 20 to 40 mL min^{-1}, after which SAC and ASAR declined with increasing flow rate. Higher flow rate leads to an increase in the ions available for adsorption, but only so long as the residence time in the flow cell is sufficiently long for the ions to migrate into the available micropore spaces of the electrodes[28].

The superior performance of flow-by CDI can likely be attribute to two factors: lower internal contact resistance and fewer faradaic side reactions. First, based on electrochemical impedance spectroscopy (EIS), the difference in electrical impedance between flow-by and flow-through CDI systems is quite pronounced (see Appendix F). Using NF electrodes, the impedance in the flow-by cell exhibited two RC time-scales rather than one. Meanwhile, the average setup resistance, $\overline{R}_S$, was lower using flow-by CDI ($\overline{R}_S = 0.5\ \Omega$) compared to flow-through ($\overline{R}_S = 1.2\ \Omega$). The two RC time scales are likely a direct consequence of the NF electrode's morphology. The NF electrode is made of dense foam
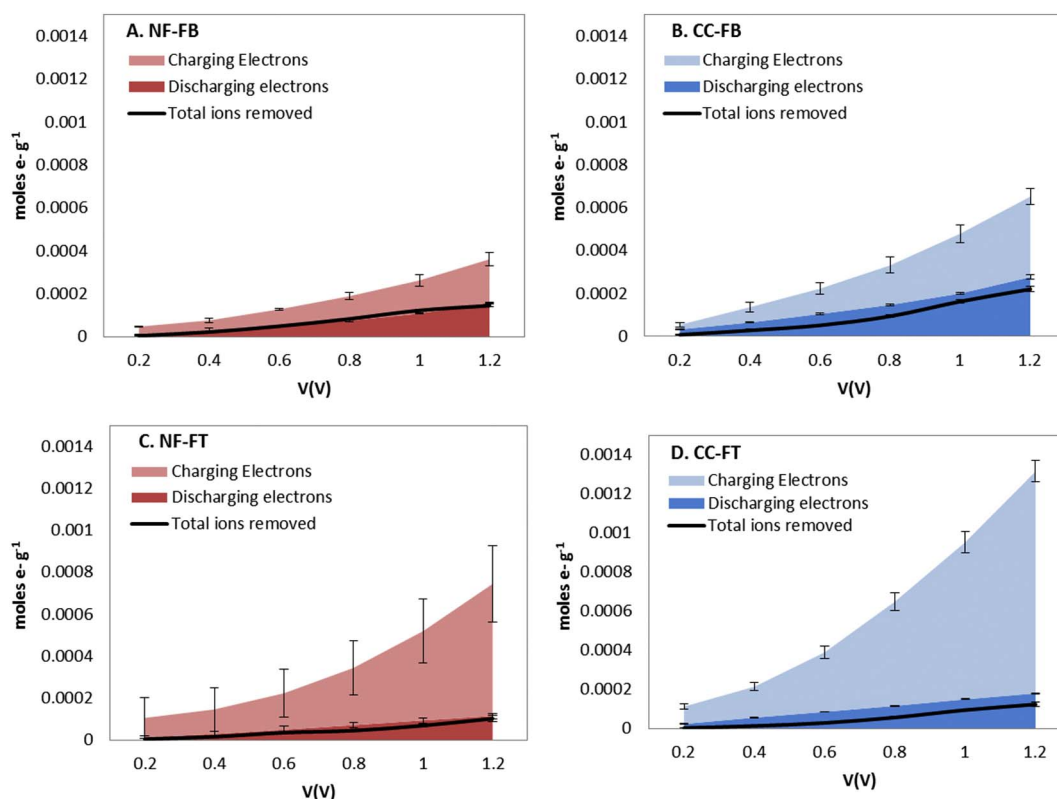

Fig. 4. Charging and discharging electron balance for A. NF-FB, B. CC-FB, C. NF-FT and D. CC-FT. All charging and discharging times were equal, HCT = 1 h, Φ = 20 mL min^{-1}, N = 3, error bars show standard deviation.

with a network of fibers and cracks permeating the material and a thin outer coating. While there is evidence that differing pore size should not influence the electrode impedance[29], the presence of the thin outer coating could lead to two distinct capacitive regimes. In the flow-through regime, the fluid can advect directly through the electrode to access the micropore spaces, but in a flow-by setup, ions must migrate first through the thin outer coating. The slow diffusive transport into the porous electrodes results in the near surface sites initially accumulating ions which then act as a barrier to ion transport to the deeper porous electrode sites. Further testing would be required in order to confirm this hypothesis although it has been previously observed for porous electrodes relying on diffusion for internal transport[30]. For the CC, both flow cells act as RC circuits with a single time constant. Nevertheless, the average setup resistance and the average contact resistance, $\overline{R}_C$, also appear lower in the flow-by ($\overline{R}_S = 0.4\ \Omega$, $\overline{R}_C = 2.7\ \Omega$) compared to flow-through ($\overline{R}_S = 1.6\ \Omega$, $\overline{R}_C = 6.0\ \Omega$). Higher resistances observed in the flow-through design may be attributed to differences in the current collector morphology and contact area. The current collector in the flow-by design was a solid rectangular foil 12.5 cm^2 or 72% of the electrode area, whereas the current collector in the flow-through design was perforated to allow for fluid transport. This ultimately increased the electrical resistance of the material and reduced the current collector area to ~8 cm^2 or 46% of the electrode (see Appendix F). High contact resistance is a major cause of electrical inefficiencies in most CDI systems [31], and this contributes to the performance disparity between flow-through and flow-by CDI. Second, flow-by CDI undergoes fewer parasitic side reactions as indicated by the charge balance presented in Fig. 4. Here, the figure depicts the specific charge of the electrodes during the charging and discharging phases of the CDI process. In an ideal, reversible process, these values would be equivalent. Nevertheless, both flow-by and flow-through CDI systems exhibit asymmetries in the specific charge measured during the charging and discharging. This delta can be attributed to irreversible side reactions occurring in the electrochemical system. Typical reactions include redox reaction with dissolved oxygen in solution, electrolysis of water, and electrode oxidation[32–34]. The difference in applied charge and discharge is lower in the flow-by system indicating lower rates of faradaic reactions. Higher degradation and side reactions in flow-through vs flow-by CDI has also been observed by others[19].

Why does flow-through CDI promote redox reactions to a greater extent than flow-by? First, flow-through cells likely produce a stronger pH response as a result of sequential ion screening. As one ion is preferentially stored in the first electrode, for example sodium ions in the cathode as shown in Fig. 5A, electrolysis occurs in the opposite electrode in order to maintain electroneutrality leading to a change in pH. This pH change can alter redox potential enabling or preventing reactions that rely on H$^+$ or OH$^-$. Changes in pH have long been observed in CDI systems and have most frequently been attributed to faradaic reactions within the electrochemical cell[32,35]. Nevertheless, acid-base reactions, including the self ionization of water, could also contribute to pH fluctuations[36]. Similarly, a second mechanism considers the dynamic nature of the feed stream in a flow-through CDI cell. Here, byproducts from faradaic reactions that occur in the first electrode are directly passed into the second electrode altering the feed composition and enabling sequential reactions to take place. An example of a possible reaction sequence is shown in Fig. 5B. Cohen et al. proposed a related mechanism for electrode instability in flow-through systems. They theorized that OH$^-$ ions produced at the negative electrode could react with the carbon in the positive electrode via: $C + 6OH^- = CO_3^{2-} + 3H_2O + 4e^-$ [19]. Furthermore, the production of OH$^-$ raises pH lowering the standard potential and increasing the driving potential for carbon electrode oxidation according to the Nernst equation. While faradaic reactions also occur in the flow-by design, the reaction kinetics are diffusion limited across the PTFE membrane and less likely to react at the opposite electrode.

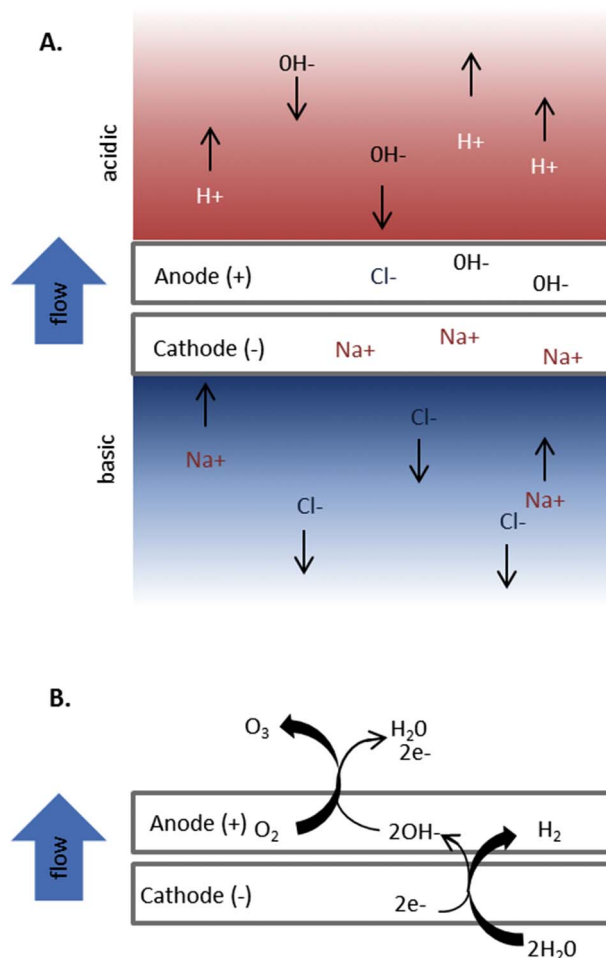Besides faradaic reactions taking place within the solution,

Fig. 5. Sequential reactions in flow-through CDI. A. Ions may be preferentially adsorbed depending on electrode order leading to a pH response in the flow cell. Here, the cathode is first in the flow path; Na$^+$ ions are stored while Cl$^-$ ions are expelled. To achieve electroneutrality, hydroxide ions are stored in the cathode reducing the amount of salt stored and decreasing effluent pH. B. Due to the sequential nature of flow-through electrodes, the feed composition into the cathode and anode are different. Products from faradaic reactions that occur in the cathode (anode) can pass through the anode (cathode) and react.

oxidation of the carbon materials could also contribute to the lower-than-expected SAC and Λ compared to theory. Indeed, the oxygen content of the electrodes increased after use in CDI, particularly when using the flow-through configuration (see Appendix D). For the NF, oxygen content increased from 2.1%O to 9.2%O (FB) and 11%O (FT), while oxygen content for the CC increased from 6.6%O to 13%O (FB) and 19%O (FT) after ~48 h of use. Furthermore, continued operation results in a dramatic decline in electrode performance for ASAR and SAC as shown in Appendix K. To better understand the degradation of the electrodes, the flow-cells were operated continuously for a 22-hour period using HCT = 5 min; details can be found in Fig. 6A. For both flow cell architectures and both carbon materials, the electrode performance decreased logarithmically over time. After 120 cycles, the SAC decreased 64% (NF-FB), 72% (NF-FT), 57% (CC-FB), and 77% (CC-FT). Although SAC decreased faster using the flow-through design, flow-through CDI yielded higher absolute salt removal than the flow-by CDI for the duration of experiment. Meanwhile, charge efficiency also decreased logarithmically with each additional charge cycle, shown in Fig. 6B. For the NF, the charge efficiency was initially higher using the flow-by configuration, but performance appeared more stable using the flow-through configuration. After 120 cycles for the NF, charge efficiency decreased by 79% using flow-by architecture compared to a 49% reduction for the flow-through. For CC, the charge efficiency appeared
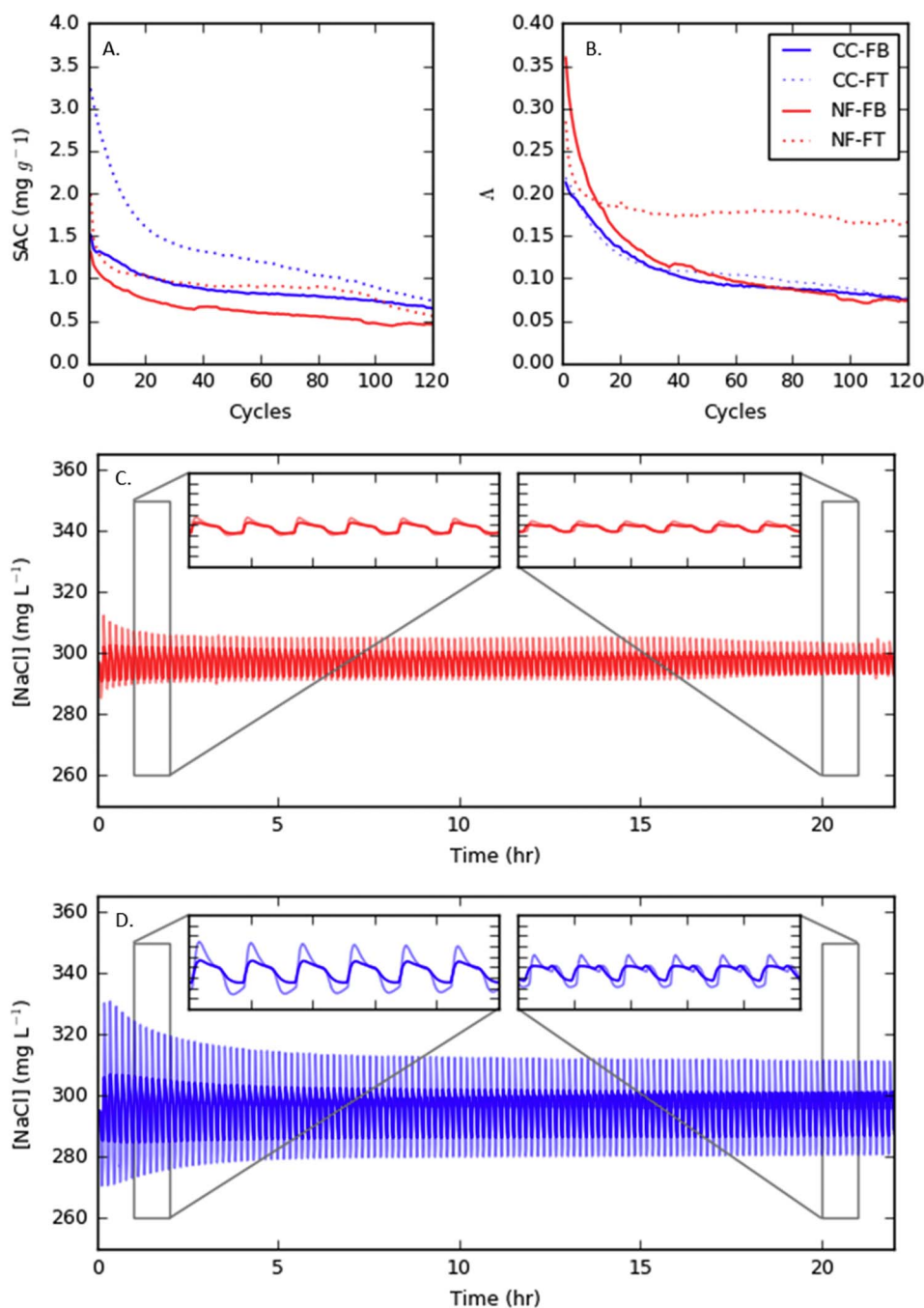
Fig. 6. Long-term CDI Performance. A. SAC decreased logarithmically over 120 cycles for NF (red) and CC (blue) using flow-through (FT) and flow-by (FB) cell architectures. CC-FB: $y = -0.188\ln(x) + 1.59$, $R^2 = 0.97$; CC-FT: $y = -0.532\ln(x) + 3.32$, $R^2 = 0.98$; NF-FB: $y = -0.174\ln(x) + 1.30$, $R^2 = 0.98$; and NF-FT: $y = -0.194\ln(x) + 1.64$, $R^2 = 0.81$. B. Charge efficiency also decreased logarithmically. CC-FB: $y = -0.034\ln(x) + 0.235$, $R^2 = 0.97$; CC-FT: $y = -0.031\ln(x) + 0.230$, $R^2 = 0.97$; NF-FB: $y = -0.056\ln(x) + 0.329$, $R^2 = 0.97$; NF-FT: $y = -0.014\ln(x) + 0.233$, $R^2 = 0.76$. C. NaCl concentration for FB (dark color) and FT (light color) CDI over a 22-hour period using NF electrodes. D. NaCl concentration for FB (dark color) and FT (light color) CDI over a 22-hour period using CC electrodes. HCT = 5 min, $\Phi = 20$ mL min^{-1}, V = 1.2 V. (For interpretation of the references to color in this figure legend, the reader is referred to the web version of this article.)

independent of operational mode; it decreased 65% after 120 cycles using either flow-by and flow-through CDI.

The development of inversion peaks, shown in Fig. 6C–D, contributed to reduction in electrode performance over time. Inversion peaks are caused by oxidation of the electrodes; oxygen moieties change the PZC of the electrode material and exacerbates co-ion repulsion upon charging[37,38]. The choice of electrode material appeared to influence the development of inversion peaks more than the cell architecture. Using NF electrodes, inversion peaks could be observed within 45 cycles (7.5 h) for flow-by CDI compared to 83 cycles (13.8 h) for flow-through, while for CC electrodes, inversion peaks developed after 30 cycles (5 h) and 10 cycles (1.6 h) for flow-by and flow-through CDI, respectively. Overall, the CC is more prone to developing inversion peaks than the NF; this is possibly due to higher initial oxygen content[39].

4. Conclusion

In general, flow-by rather than flow-through CDI cell architecture yields superior performance including higher SAC for a given HCT, higher charge efficiency, and improved electrode stability. The performance advantage can be attributed to

1. Lower setup resistance and contact resistance during operation;
2. Fewer faradaic side reactions, and consequently, less electrode oxidation.

Nevertheless, device performance is sensitive to a number of operational parameters including voltage, HCT, and flow rate. Higher voltage tends to improve salt removal, but it also increases faradaic side reactions and electrode oxidation that disproportionally affect the flow-through design. Meanwhile, longer HCT and higher flow rates yield

better SAC and ASAR for the flow-by CDI. In flow-through CDI, optimal performance occurs with higher flow rate and shorter HCT (< 5 min). Moreover, differences in setup resistance and contact resistance may be more related to cell build rather than a true limitation of cell architecture; i.e. careful design and construction may help to overcome the high resistances observed in the flow-through cell architecture.

Additionally, the choice of electrode material plays a critical role, particularly in determining the amount of salt stored during CDI. First, the micropore volume dictates the total salt storage capacity of the material. Second, the macropore spaces control accessibility to the micropore volumes. Materials with higher macroporosity are more sensitive to changes in cell architecture.

Overall, this study shows that CDI operational design and electrode selection can strongly influence observed performance. As researchers continue to develop new materials and better designs for CDI, it is important that all experimental parameters are reported and that the system is optimized across voltage, HCT, and flow rate. Efforts to standardize reporting metrics should continue, and future models should aim to include parameters for electrode macroporosity and the effects of oxidation.

Acknowledgments

Appendix A. Supplementary data

Supplementary data to this article can be found online at https://doi.org/10.1016/j.desal.2018.01.018.

References

[1] J. Gunderson, High-purity Water: Demanding Requirements Drive Treatment Advancements in Ultrapure Water Production, http://www.waterworld.com/articles/iww/print/volume-_14/issue-_5/features/high-_purity-_water-_demanding-_requirements-_drive_treatment-_advancements-_in-_ultrapure.html. Accessed: 2017-09-08.

[2] M. Atabab, J. Smallbone, A. Roskillya, An operational and economic study of a reverse osmosis desalination system for potable water and land irrigation, Desalination 397 (2016) 174184.

[3] M. Elimelech, W.A. Phillip, The future of seawater desalination: energy, technology, and the environment, Science 333 (2011) 712–717.

[4] J.R. Werber, A. Deshmukh, M. Elimelech, The critical need for increased selectivity, not increased water permeability, for desalination membranes, Environ. Sci. Technol. Lett. 3 (2016) 112–120.

[5] M. Barakat, New trends in removing heavy metals from industrial wastewater, Arab. J. Chem. 4 (2011) 361–377.

[6] S. Porada, B.B. Sales, H.V.M. Hamelers, P.M. Biesheuvel, Water desalination with wires, J. Phys. Chem. Lett. 3 (2012) 1613–1618 PMID: 26285717.

[7] P. Długołecki, A. Van Der Wal, Energy recovery in membrane capacitive deionization, Environ. Sci. Technol. 47 (2013) 4904–4910.

[8] R. Zhao, S. Porada, P.M. Biesheuvel, A. Van der Wal, Energy consumption in membrane capacitive deionization for different water recoveries and flow rates, and comparison with reverse osmosis, Desalination 330 (2013) 35–41.

[9] R. Zhao, M. Van Soestbergen, H. Rijnaarts, A. Van der Wal, M. Bazant, P. Biesheuvel, Time-dependent ion selectivity in capacitive charging of porous electrodes, J. Colloid Interface Sci. 384 (2012) 38–44.

[10] M.E. Suss, Size-based ion selectivity of micropore electric double layers in capacitive deionization electrodes, J. Electrochem. Soc. 164 (2017) E270–E275.

[11] S.-J. Seo, H. Jeon, J.K. Lee, G.-Y. Kim, D. Park, H. Nojima, J. Lee, S.-H. Moon, Investigation on removal of hardness ions by capacitive deionization (CDI) for water softening applications, Water Res. 44 (2010) 2267–2275.

[12] T. Ryu, J.C. Ryu, J. Shin, D.H. Lee, Y.H. Kim, K.-S. Chung, Recovery of lithium by an electrostatic field-assisted desorption process, Ind. Eng. Chem. Res. 52 (2013) 13738–13742.

[13] T. Ryu, D.-H. Lee, J.C. Ryu, J. Shin, K.-S. Chung, Y.H. Kim, Lithium recovery system using electrostatic field assistance, Hydrometallurgy 151 (2015) 78–83.

[14] M. Bryjak, A. Siekierka, J. Kujawski, K. Smolinska-Kempisty, W. Kujawski, Capacitive deionization for selective extraction of lithium from aqueous solutions, J. Membrane Separation Technol. 4 (2015) 110.

[15] S. Porada, D. Weingarth, H.V.M. Hamelers, M. Bryak, V. Presser, P.M. Biesheuvel, Carbon flow electrodes for continuous operation of capacitive deionization and capacitive mixing energy generation, J. Mater. Chem. A 2 (2014) 9313–9321.

[16] M.E. Suss, T.F. Baumann, W.L. Bourcier, C.M. Spadaccini, K. a. Rose, J.G. Santiago, M. Stadermann, Capacitive desalination with flow-through electrodes, Energy Environ. Sci. 5 (2012) 9511.

[17] Y. Liu, C. Nie, X. Liu, X. Xu, Z. Sun, L. Pan, Review on carbon-based composite materials for capacitive deionization, RSC Adv. 5 (2015) 15205–15225.

[18] S. Porada, R. Zhao, A. Van Der Wal, V. Presser, P.M. Biesheuvel, Review on the science and technology of water desalination by capacitive deionization, Prog. Mater. Sci. 58 (2013) 1388–1442.

[19] I. Cohen, E. Avraham, Y. Bouhadana, A. Soffer, D. Aurbach, The effect of the flow-regime, reversal of polarization, and oxygen on the long term stability in capacitive de-ionization processes, Electrochim. Acta 153 (2015) 106–114.

[20] A. Hemmatifar, M. Stadermann, J.G. Santiago, Two-dimensional porous electrode model for capacitive deionization, J. Phys. Chem. C 119 (2015) 24681–24694.

[21] T. Mallouk, Making and cleaning a Pt working electrode, http://courses.chem.psu.edu/chem524/Pt_electrode_expt0.pdf/. Accessed: 2017-09-08.

[22] N. Elgrishi, K.J. Rountree, B.D. McCarthy, E.S. Rountree, T.T. Eisenhart, … , A practical beginners guide to cyclic voltammetry, J. Chem. Educ. (2017), http://pubs.acs.org/doi/abs/10.1021/acs.jchemed.7b00361.

[23] M.E. Suss, S. Porada, X. Sun, P.M. Biesheuvel, J. Yoon, V. Presser, Water desalination via capacitive deionization: what is it and what can we expect from it? Energy Environ. Sci. 8 (2015) 2296–2319.

[24] P.M. Biesheuvel, S. Porada, M. Levi, M.Z. Bazant, Attractive forces in microporous carbon electrodes for capacitive deionization, J. Solid State Electrochem. 18 (2014) 2044–2078.

[25] S. Porada, L. Borchardt, M. Oschatz, M. Bryjak, J.S. Atchison, K.J. Keesman, S. Kaskel, P.M. Biesheuvel, V. Presser, Direct prediction of the desalination performance of porous carbon electrodes for capacitive deionization, Energy Environ. Sci. 6 (2013) 3700.

[26] X. Gao, J. Landon, J.K. Neathery, K. Liu, Modification of carbon xerogel electrodes for more efficient asymmetric capacitive deionization, J. Electrochem. Soc. 160 (2013) E106–E112.

[27] T. Kim, J. Yoon, CDI ragone plot as a functional tool to evaluate desalination performance in capacitive deionization, RSC Adv. 5 (2015) 1456–1461.

[28] P. Liu, H. Wang, T. Yan, J. Zhang, L. Shi, D. Zhang, Grafting sulfonic and amine functional groups on 3D graphene for improved capacitive deionization, J. Mater. Chem. A 4 (2016) 5303–5313.

[29] M.E. Suss, T.F. Baumann, M.A. Worsley, K.A. Rose, T.F. Jaramillo, M. Stadermann, J.G. Santiago, Impedance-based study of capacitive porous carbon electrodes with hierarchical and bimodal porosity, J. Power Sources 241 (2013) 266–273.

[30] G. Gao, C.D. Vecitis, Reactive depth and performance of an electrochemical carbon nanotube network as a function of mass transport, ACS Appl. Mater. Interfaces 4 (2012) 6096–6103 PMID: 23106549.

[31] Y. Qu, T.F. Baumann, J.G. Santiago, M. Stadermann, Characterization of resistances of a capacitive deionization system, Environ. Sci. Technol. 49 (2015) 9699–9706 PMID: 26214554.

[32] C. Zhang, D. He, J. Ma, W. Tang, T.D. Waite, Faradaic reactions in capacitive deionization (CDI) - problems and possibilities: a review, Water Res. 128 (2018) 314–330.

[33] N. Holubowitch, A. Omosebi, X. Gao, J. Landon, K. Liu, Quasi-steady-state polarization reveals the interplay of capacitive and faradaic processes in capacitive deionization, ChemElectroChem 4 (2017) 2404–2413.

[34] B. Shapira, E. Avraham, D. Aurbach, Side reactions in capacitive deionization (CDI) processes: the role of oxygen reduction, Electrochim. Acta 220 (2016) 285–295.

[35] D. He, C. Eng Wong, W. Tang, P. Kovalsky, T.D. Waite, Faradaic reactions in water desalination by batch-mode capacitive deionization, Environ. Sci. Technol. Lett. 3 (2016) 222–226.

[36] J. Dykstra, K. Keesman, P. Biesheuvel, A. van der Wal, Theory of pH changes in water desalination by capacitive deionization, Water Res. 119 (2017) 178–186.

[37] Y. Bouhadana, E. Avraham, M. Noked, M. Ben-Tzion, A. Soffer, D. Aurbach, Capacitive deionization of NaCl solutions at non-steady-state conditions: inversion functionality of the carbon electrodes, J. Phys. Chem. C 115 (2011) 16567–16573.

[38] P. Biesheuvel, H. Hamelers, M. Suss, Theory of water desalination by porous electrodes with immobile chemical charge, Colloids Interface Sci. Communications 9 (2015) 1–5.

[39] E.N. Guyes, A. Simanovski, M.E. Suss, Several orders of magnitude increase in the hydraulic permeability of flow-through capacitive deionization electrodes via laser perforations, RSC Adv. 7 (2017) 21308–21313.